Journal of Materials Research and Technology 30 (2024) 348–359

Contents lists available at ScienceDirect

Journal of Materials Research and Technology

journal homepage: www.elsevier.com/locate/jmrt

In-situ mechanical and microstructural characterization of miniaturized Al-Mg-Sc-Zr and AlSi10Mg specimens processed by laser powder-bed fusion (PBF-LB)

Laura Cordova [a,b,*], Ton Bor [a], Eric Macía Rodríguez [b], Tiedo Tinga [a], Mónica Campos [b]

[a] Department of Mechanics of Solids, Surfaces & Systems (MS3), University of Twente, Drienerlolaan 5, 7522 NB, Enschede, Netherlands
[b] Department of Materials Science and Engineering, University Carlos III of Madrid, Avda. Universidad, 30, 28911, Leganés, Spain

ARTICLE INFO

Handling editor: L Murr

Keywords:
Powder bed fusion laser-beam (PBF-LB)
Anisotropy
Mechanical properties
Al-Mg-Sc-Zr
AlSi10Mg
Scalmalloy®

ABSTRACT

Manufacturing through powder-bed fusion laser-beam (PBF-LB) enables innovative part design strategies, facilitating weight reduction, and capitalizing on the metallurgical conditions developed during the manufacturing of designed alloys. Consequently, Al-based light alloys hold enormous potential for reducing fuel consumption in the transport industry. Fabricating such small features has a significant impact on heat dissipation, thereby affecting microstructure, porosity, and, consequently, mechanical properties. This study proposes the use of near-net shape miniaturized tensile specimens in both horizontal and vertical orientations to characterize Al-Mg-Sc-Zr, commercially known as Scalmalloy®, and AlSi10Mg, two aluminum alloys typically employed in PBF-LB. The size and distribution of both grains and pores were analyzed and compared, with Al-Mg-Sc-Zr exhibiting a more competitive set of properties compared to AlSi10Mg. This difference also influences mechanical properties. Al-Mg-Sc-Zr demonstrated double the Ultimate Tensile Strength (UTS) of AlSi10Mg (450 MPa versus 225 MPa) and higher hardness values (142 HV30 versus 75 HV30), with similar elongation in both alloys (approximately 12–16%), owing to its fine microstructure and low porosity of the near-net shape miniaturized tensile specimens. Neither material exhibited any form of anisotropy. In-situ SEM tensile tests were conducted to monitor damage evolution, allowing continuous observation of crack nucleation and propagation through imperfections typically encountered in PBF-LB. Despite differences in static strength, the fracture surfaces of the samples displayed a ductile behavior in both materials.

1. Introduction

The powder-bed fusion laser-beam (PBF-LB) process, belonging to the metal additive manufacturing (AM) group of processes, is extensively utilized for fabricating aerospace components, where factors such as weight reduction, high dimensional accuracy, and complexity significantly influence performance [1]. Despite its development, processing aluminum alloys via the PBF-LB process has posed challenges due to their high reflectivity and poor flowability [2].

AlSi10Mg, a widely used casting alloy, exhibits excellent weldability due to its near eutectic composition of aluminum and silicon, along with high corrosion resistance. The addition of low amounts of magnesium (0.3–0.5 wt%) induces an age-hardening effect through the formation of Mg_2Si precipitates [3,4]. Its attractive mechanical properties and low weight make this alloy suitable for numerous applications, particularly in the automotive and aerospace industry where alloys like Al7075 are commonly employed. However, precipitation hardening alloys from the 2xxx and 7xxx series exhibit high susceptibility to cracking due to large solidus-liquidus temperature ranges [5].

Al-Mg-Sc-Zr alloy, commercially known as Scalmalloy®, is a scandium-modified aluminum alloy developed by Airbus Group Innovations for aerospace applications with enhanced mechanical performance. Scandium addition to aluminum alloys also improves processability. Typically, Sc-containing alloys rely on precipitation hardening to enhance strength, with conventional processing involving controlled ageing during which ordered and coherent Al_3Sc precipitates form a supersaturated solid solution of Sc. In the case of PBF-LB, the process itself can precipitate Al3Sc, preventing recrystallization, refining grains effectively, and acting as an age-hardener, resulting in high strength [6]. Scandium is also reported to increase the weldability

* Corresponding author. Department of Mechanics of Solids, Surfaces & Systems (MS3), University of Twente, Drienerlolaan 5, 7522 NB, Enschede, Netherlands.
E-mail address: lcordova@ing.uc3m.es (L. Cordova).

https://doi.org/10.1016/j.jmrt.2024.03.084
Received 3 January 2024; Received in revised form 13 March 2024; Accepted 13 March 2024
Available online 16 March 2024

Table 1
Chemical composition (wt%) of the studied aluminum alloys.

Material	Al	Si	Mg	Sc	Zr	Fe	Mn	Ni	Ti	V
AlSi10Mg	Bal.	10.10	0.38	–	–	0.11	<0.01	<0.01	<0.01	–
Al-Mg-Sc-Zr	Bal.	<0.01	4.39	0.66	0.31	0.13	0.49	–	0.021	0.013

of aluminum alloys, particularly for those prone to hot cracking and extended heat-affected zone formation [7].

One of the primary challenges in manufacturing aluminum alloys via PBF-LB is the typically high level of porosity obtained, which often compromises mechanical properties [8]. Thermal stresses, commonly observed, can cause distortions and hot cracking in parts. Pre-heating the powder bed is a potential solution [9,10]. During the processing of aluminum alloys, melt pool solidification may lead to oxide formation on the layer surface, resulting in defects such as pores and deposition of unmelted powder [11]. Porosity in PBF-LB parts arise from lack of fusion or material overheating-induced turbulences in the melt pool (e.g., keyhole pores and metallurgical pores) [10]. Laser heat input, a crucial parameter, determines the degree of consolidation in powder particles. Volumetric energy density (E_v) typically represents the heat input received by the powder bed, calculated based on influential process parameters such as power, speed, hatch space, and layer thickness.

When the metal powder melts under the laser, a melt pool forms. Excessive energy during melting can lead to porosity formation due to keyhole instabilities and gas entrapment. Contaminant gases present, like hydrogen or oxygen from powder humidity, or argon used as protective gas during PBF-LB, can form bubbles within the molten metal. Marangoni convection [12] induces melt pool movement based on molten metal surface tension, as described by Olakanmi [13], potentially transporting bubbles towards the surface, as studied by Hojjatzadeh et al. [14]. However, upon solidification, bubbles remain entrapped, forming spherical pores. Large and irregular pores are detrimental to mechanical properties as they can initiate cracks. Weingarten et al. [15] and Li et al. [16] demonstrated significant reduction in hydrogen porosity through pre-drying treatments. Understanding porosity formation during and after laser melting enables process optimization, potentially reducing porosity.

Shakil et al. [17] compared the microstructure and micro- and macro-mechanical properties of Scalmalloy. Nano-indentation was used to study micro-mechanical properties, with micro and macro analyses concluding little to no anisotropy in samples built horizontally and vertically. To date, mechanical properties of PBF-LB processed aluminum alloys have been studied using macro-mechanical tests and micro/nano-indentations. However, utilizing miniaturized specimens enables closer exploration of porosity effects and microstructural variations [18]. For instance, Torralba et al. [19] investigated the role of porosity and microstructure on mechanical properties of sintered steels using miniaturized tensile test specimens, providing further insights into fracture mechanics. Their study concluded that cracks initiate around pores, with sharper pores having more significant effects as crack initiators, propagating through grain boundaries and phase interfaces.

This study aims to evaluate the mechanical properties of pre-dried Al-Mg-Sc-Zr alloy and AlSi10Mg alloy, utilizing miniaturized specimens. This approach allows for determination of local mechanical properties in small, complex part features, and facilitates in-situ testing. The latter offers the opportunity to closely examine the effect of porosity and inclusions on fracture behavior of both aluminum alloys. Hence, this paper contributes by (i) testing mechanical properties of pre-dried Al-Mg-Sc-Zr and AlSi10Mg materials, and (ii) demonstrating the benefits of miniaturized tensile specimens and in-situ testing for characterizing AM parts.

2. Materials and methods

The compositions of the Al-Si-Mg and Al-Mg-Sc-Zr (Scalmalloy®) powders used to manufacture test specimens via the PBF-LB process are listed in Table 1. The studied aluminum alloys have a theoretical density of approximately 2.7 g/cm^3.

The particle size distribution (PSD) and morphology of the powder significantly influence PBF-LB processing [20]. Fig. 1 illustrates the morphology of the aluminum powders and the PSD, which was measured using a laser particle size analyzer (Mastersizer 2000). While powder particles in both alloys exhibit a spherical shape, there are notable differences in morphology. AlSi10Mg displays a rougher surface and a higher number of satellites, as discussed in a previous study Cordova et al. [21]. The size distribution of the raw powders follows a similar trend (slightly finer for Al-Mg-Sc-Zr) with an average particle size (d50) of about 34 μm and 38 μm for AlSi10Mg powders.

Miniaturized tensile test specimens of AlSi10Mg and Al-Mg-Sc-Zr were manufactured in horizontal (H) and vertical (V) directions using the PBF-LB SLM Solutions 280HL machine (SLM Solutions GmbH). The process was conducted under a controlled inert atmosphere using argon gas to prevent oxidation. Fig. 2a and b illustrate the geometry of the test specimens, the as-built specimens, and the support structures linking the specimens to the build plate.

Preceding the building job, an overnight (12-h) vacuum drying process was conducted to reduce the moisture level of the metal powders, aiming to improve powder spreadability and decrease hydrogen porosity. The printing parameters used to construct the specimens were optimized to achieve maximum specimen density. Both materials were built on a preheated build plate at 150 °C using a laser power of 380 W. The volumetric energy densities (J/mm^3) applied to each material are presented in Table 2. In a study on optimal process parameters for AlSi10Mg, Read et al. [22] concluded that using a Concept Laser M2

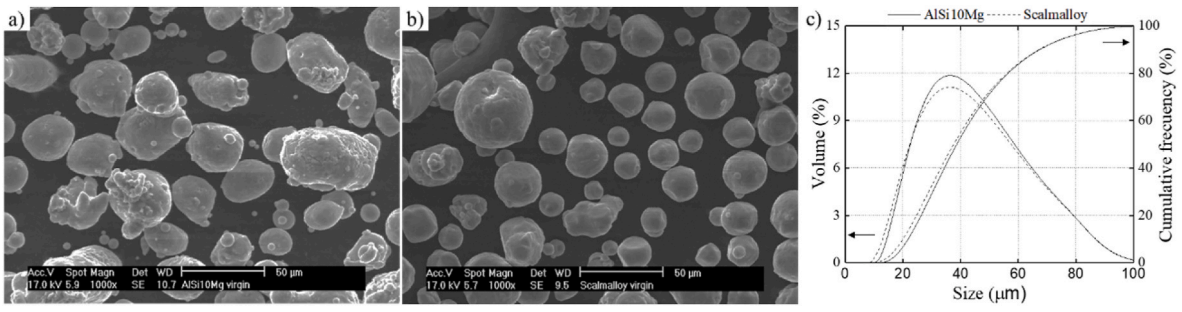

Fig. 1. SEM micrograph of a) AlSi10Mg and b) Al-Mg-Sc-Zr powders. c) Particle size distribution (PSD) of AlSi10Mg and Al-Mg-Sc-Zr powders. The PSD plots contain curves representing the occurrence (left) and cumulative frequency (right) of the different particle sizes.

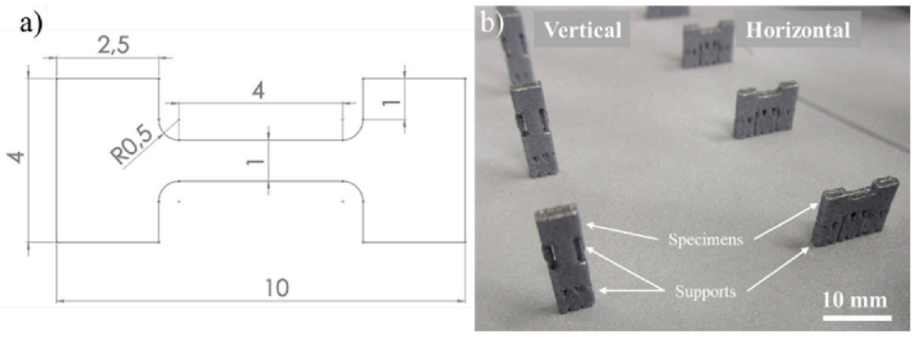

Fig. 2. (a) Geometry of the miniaturized tensile test specimens with dimensions in mm, 1 mm thickness, (b) PBF-LB manufactured specimens built in horizontal and vertical building directions on the build plate with support structures attached.

Table 2
Energy density (J/mm^3) applied during the PBF-LB process to AlSi10Mg and Al-Mg-Sc-Zr powders.

Materials	E_v (J/mm^3)
AlSi10Mg	43.8
Al-Mg-Sc-Zr	78.0

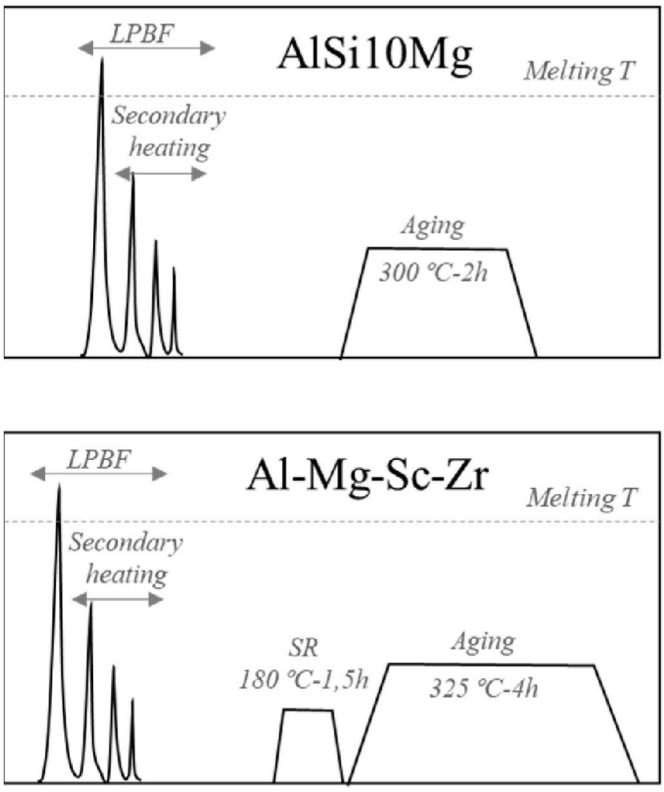

Fig. 3. Thermal cycles during the SLM process and post-processing for AlSi10Mg and Al-Mg-Sc-Zr alloys.

Cusing® SLM machine with a maximum laser power of 200 W would result in an optimal $E_v = 60$ J/mm^3. Low energy densities (<50 J/mm^3) resulted in lack of fusion porosity while higher energy densities than optimal showed scattered porosity such as keyhole formation. However, using an EOS M290 machine with a maximum laser power of 400 W, Maamoun et al. [23] utilized an optimal energy density of 49.9 J/mm^3, a value closer to that selected for this study under similar process conditions.

For the Al-Mg-Sc-Zr alloy composition, Spierings et al. [24] investigated the processing window of this material. Their study demonstrated a relative density >99% in a range of E_v between 75 J/mm^3 and 240 J/mm^3. The investigation was conducted using a ConceptLaser M2 machine equipped with a 200 W Nd-YAG laser.

The build platform preheating temperature, hatch scanning pattern, geometry, and support size were kept the same for both materials. The specimens were built with a layer thickness of approximately 50 μm. After removal of the specimens from the build plate, the AlSi10Mg specimens underwent heat treatment at 300 °C for 2 h. The Al-Mg-Sc-Zr specimens were subjected to a stress relief treatment of 1.5 h at 180 °C, followed by a precipitation hardening treatment of 4 h at 325 °C, as depicted in Fig. 3. The latter treatment is essential as the strength of Al-Mg-Sc-Zr primarily relies on precipitation hardening. The heat treatments are expected to significantly influence the mechanical properties of both materials. Indeed, Li et al. [25] reported a substantial decrease of 35% in the tensile strength of AlSi10Mg, accompanied by a notable increase in ductility of 60%, following solution heat treatment (at 450 °C for 2 h). Conversely, after a similar heat treatment of as-printed Al-Mg-Sc-Zr parts, Spierings et al. [26] and Schmidtke et al. [27] reported an increase in the tensile strength.

First, the aluminum powders were analyzed using a scanning electron microscope (SEM, model Jeol JSM-7200 F) and the particle size distribution (PSD) was obtained by laser diffraction (Mastersizer 2000), following ASTM B 822-02. Second, an optical microscope (Keyence VHX-5000) and a scanning electron microscope (SEM, model FEI Teneo) were employed to study the microstructure and porosity of the printed specimens after conventional metallographic preparation. The aluminum alloys were etched with Keller's reagent for 20 s to reveal the microstructure. Crystal orientation and grain size distribution were determined using electron backscatter diffraction (EBSD) and analyzed with software AZtecHKL from Oxford Instruments. The AlSi10Mg and Al-Mg-Sc-Zr powders, as well as specimens built in the horizontal (H) and vertical direction (V), were subjected to X-ray diffraction (XRD, model X'Pert from Philips) to identify the phases present. The XRD results were processed using X'Pert HighScore software. Porosity distribution and shape parameters of the pores were obtained from the specimens' cross-sections using image analysis techniques (VHX analyzer and ImageJ software programs) and applying equations (1) and (2). The resulting pore shape (f_{shape}, i.e. aspect ratio) and circularity ($f_{circular}$) values provide insight into the type of porosity present in the specimens. The closer the f_{shape} and $f_{circular}$ values are to 1, the more spherical the pore is. The combination of these two parameters offers a measure of pore geometry.

$$f_{shape} = \frac{minD}{maxD};\ \{f_{shape} \in \mathbb{Q} \mid 0 < f_s < 1\} \tag{1}$$

$$f_{circular} = \frac{4\pi A}{P^2};\ \{f_{circular} \in \mathbb{Q} \mid 0 < f_c < 1\} \tag{2}$$

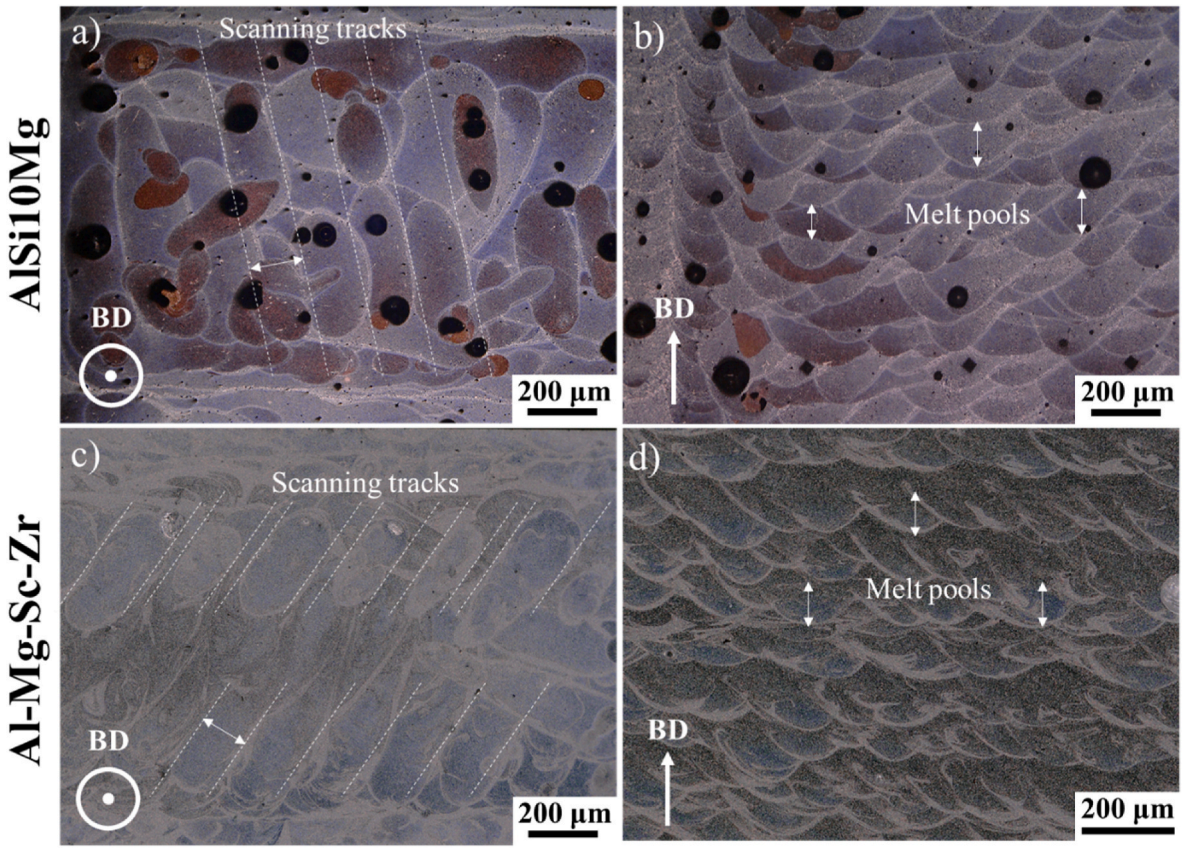

Fig. 4. Cross-sections of AlSi10Mg and Al-Mg-Sc-Zr samples perpendicular to building direction (a, c) and parallel to the building direction (b, d). Scanning tracks are shown in a) and c); melt pools are indicated in b) and d). Both materials were etched with a Keller solution for 15–20 s and the images were taken using an optical microscope.

where *minD* is the minimum pore diameter, *maxD* the maximum pore diameter, *A* the cross-sectional area and *P* the perimeter of the pore. The diameters are obtained as Ferret diameters with the image analysis techniques mentioned above.

Here's the corrected version:

"where minD is the minimum pore diameter, maxD is the maximum pore diameter, A is the cross-sectional area, and P is the perimeter of the pore. The diameters are obtained as Ferret diameters using the image analysis techniques mentioned above.

Finally, the mechanical properties were studied by conducting tensile and hardness testing to compare the performance of AlSi10Mg and Al-Mg-Sc-Zr in the horizontal (H) and vertical (V) building directions. Fig. 2a depicts the miniaturized dog-bone shaped geometry of the specimens, with a thickness of 1 mm. This specimen size allows for observation of fracture behavior inside the SEM, while also reducing production costs and printing times. Due to the high roughness of PBF-LB specimens, they were polished with silicon carbide (SiC) paper, diamond solution, and colloidal silica suspension to achieve a smoother surface.

Tensile tests were conducted using a Kammrath & Weiss GmbH micro-machine with a load of 1 kN, adjusted to a speed of 2 µm/s. One specimen of each condition was studied inside the SEM using the micro-machine. From the ex-situ tests using the micro-machine, the Ultimate Tensile Strength (UTS) was calculated as the maximum values on the engineering stress-strain curve. The elongation at break values were determined from the ratio between varied length and initial length after the specimen breakage. This in-situ test enabled monitoring of crack initiation and propagation during tensile loading. Following the tensile tests, the fracture surfaces of the specimens were examined in the SEM to facilitate understanding of the fracture behavior of the materials.

The LECO AMH 43 automatic micro-indentation testing system was utilized to compare the hardness of AlSi10Mg and Al-Mg-Sc-Zr specimens.

Five indentations at each condition were made on the clamping area of the specimens after the tensile test, following the ASTM Standard Test Method for Vickers Hardness of Metallic Materials (E 92 – 82). The specimens were embedded in epoxy resin and polished to a 'mirror-like' surface before the indentations were applied. Since the aluminum alloys studied are highly ductile, the indenter was loaded to only 3 N ($HV_{0.3}$). A patented visual PANOPTIC method automatically traced the sample edge of a live image, enabling positioning of indents and patterns directly onto the overview image of a part.

3. Results and discussion

3.1. Microstructure

Morphological differences between the two studied alloys are evident, as observed from the optical micrographs in Fig. 4, depicting the optical characterization of the etched aluminum alloys in cross-sections perpendicular and parallel to the building direction. The fine grain size distribution resulting from the rapid cooling of the PBF-LB process, along with the porosity formed due to gas entrapment, rapid solidification, and/or lack of fusion, in addition to the presence of precipitates, will be decisive factors for the mechanical properties. Fig. 4 also illustrates the scan track and melt pool distribution of AlSi10Mg and Al-Mg-Sc-Zr.

One of the most notable differences between the alloys is the pore size and distribution. AlSi10Mg exhibits the largest pores, which are predominantly spherical and located at the bottom of the melt pools

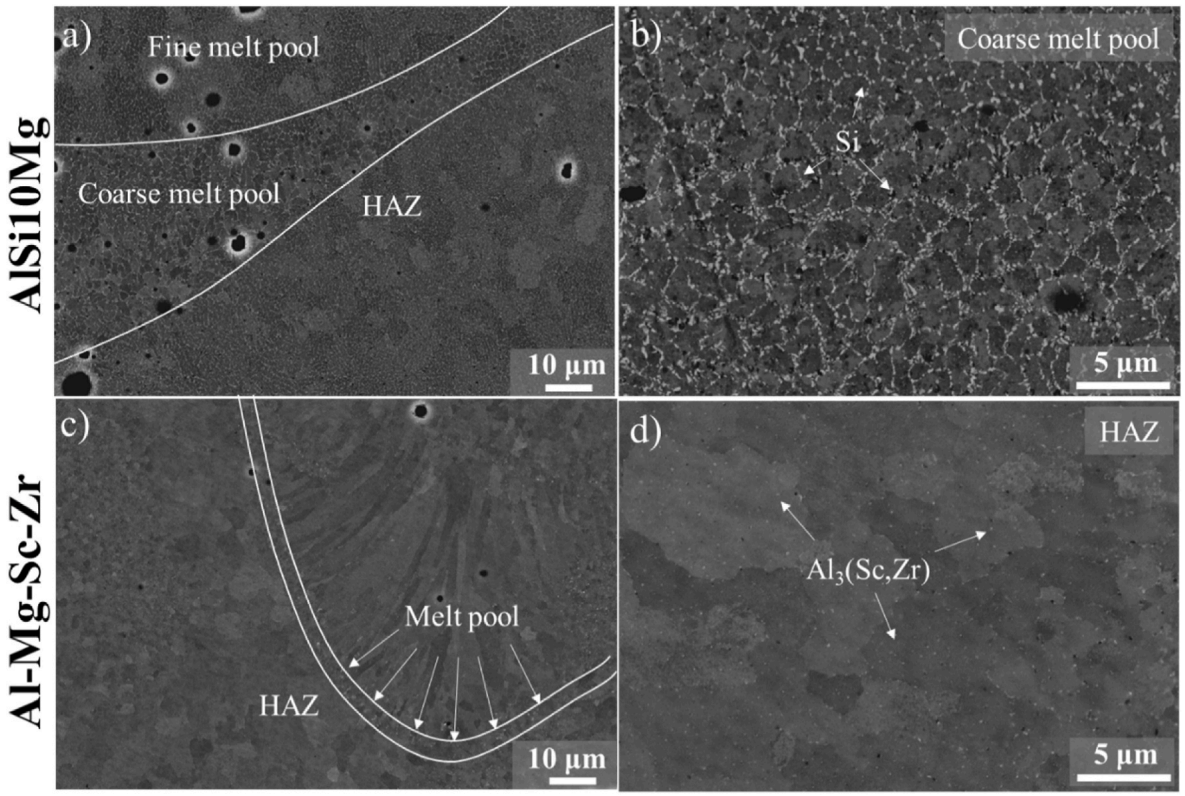

Fig. 5. SEM micrographs parallel to the building direction of a) AlSi10Mg and c) Al-Mg-Sc-Zr. b) Detail of the Si network in the coarse melt pool for AlSi10Mg and d) of the HAZ in Al-Mg-Sc-Zr where the $Al_3(Sc,Zr)$ is indicated by arrows. In this case only AlSi10Mg was etched with a Keller solution to reveal the Si phase.

(Fig. 4b). As described by Bayat et al. [28], the keyhole represents a highly unstable regime that leads to the formation of porosities at the bottom of the melt pools, as observed for AlSi10Mg in Fig. 4a–b. The pores acquire a spherical shape due to hydrostatic pressure when captured by the solidification front. In another study, Kan et al. [29] found similar porosity levels for AlSi10Mg using a comparable set of process parameters and pre-heating temperature ($E_v = 44.27$ J/mm^3 and $T = 150$ °C).

More detailed microstructural features are revealed by the SEM micrographs in the proximities of the melt pools in Fig. 5. In both materials, there are three different zones discernible across the melt pools, which could be identified based on the morphology and size of the cellular dendrites. However, these zones exhibit different characteristics for both materials.

In the microstructure of AlSi10Mg, there are three distinct regions (Fig. 5a): a fine melt pool zone, a coarse melt pool zone, and a heat-affected zone (HAZ) [23]. The fine melt pool zone, comprising most of the melt pool, is where cellular dendrites converge towards the center of the laser track. The coarse melt pool zone marks the boundary of the melt pool. The HAZ refers to a previously solidified layer affected by the heat applied to melt the powder of the new layer. In all three zones, the Si phase displays a fibrous network, as observed by Liu et al. [30].

For Al-Mg-Sc-Zr, the melt pool area is also characterized by elongated or coarse grains growing towards the center of the laser tracks (Fig. 5c). Along the border of the melt pools, fine equiaxed grains with bright precipitates are observed. According to a study on the relationship between scan speed and fine coherent Al_3Sc precipitation [31], Sc content remains in supersaturated solid solution at high scan speeds (low energy density for a given laser power). However, at lower scan speeds, Al_3Sc precipitates at the grain boundaries, acting as pinning particles. The width of this zone of fine grains is approximately 5 µm. The HAZ contains larger equiaxed grains with nanometer-sized precipitates of Al_3 (Sc,Zr), as depicted in Fig. 5d. Given the presence of Fe at approximately 0.1 wt% in both alloys, the precipitation of Al_6(Fe,Mn), especially in the case of Al-Mg-Sc-Zr with higher content of Fe and Mn, is feasible according to the equilibrium phase diagram presented using Thermo-Calc Software by Turani et al. [32]. The impact of these precipitates on the mechanical properties becomes noticeable when the composition of Al-Mg-Sc-Zr is reinforced with 1.8 wt% of Fe.

In summary, both Al-Mg-Sc-Zr and AlSi10Mg alloys exhibit an α-Aluminum solid solution as the primary phase and form precipitates. However, due to differences in composition and alloying elements between them, the nature of these precipitates varies. The high silicon content in AlSi10Mg facilitates the formation of Mg_2Si precipitates, which significantly contribute to strengthening the alloy. Conversely, the presence of scandium and zirconium in Al-Mg-Sc-Zr allows for the precipitation of $Al_3(Sc,Zr)$ phases. Furthermore, heat treatments applied to both alloys play a crucial role in promoting the formation of the aforementioned precipitates, thereby influencing their mechanical properties.

The grain size distribution in the two alloys was measured using EBSD. The differences between AlSi10Mg and Al-Mg-Sc-Zr in both horizontal and vertical geometries with a view parallel to the building direction are illustrated in Fig. 6a–d. Al-Mg-Sc-Zr exhibits finer, and narrower grains compared to AlSi10Mg, particularly between the melt pool and the HAZ. The average size of the equiaxed grains distributed along the melt pool boundaries is < 5 µm. This fine grain structure is attributed to the near-eutectic scandium content, which facilitates nucleation of strengthening phases and inhibits recrystallization, leading to grain refinement [33].

The grain size histograms obtained by EBSD are depicted in Fig. 6e. The average grain size of Al-Mg-Sc-Zr is 2.3 µm, nearly four times smaller than that of AlSi10Mg. The fine microstructure of Al-Mg-Sc-Zr is achieved through the combination of scandium and rapid solidification from the PBF-LB process. In comparison, AlSi10Mg, which underwent laser processing using optimized parameters and heat treatment to

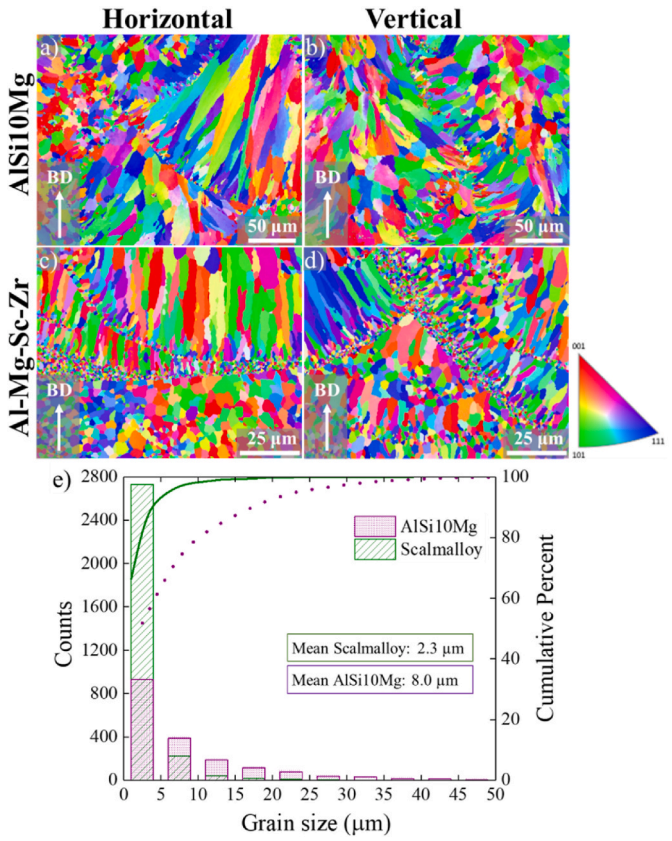

Fig. 6. Overview of the microstructure obtained by EBSD for AlSi10Mg in (a) horizontal, (b) vertical direction and Al-Mg-Sc-Zr in (c) horizontal, (d) vertical direction. Notice that the magnification for Al-Mg-Sc-Zr is twice that for AlSi10Mg. (e) Grain size distribution plots, including mean grain size values.

enhance mechanical properties, exhibits a microstructure approximately 3.5 times coarser than that of Al-Mg-Sc-Zr.

The XRD spectra of the raw powder and the printed parts of AlSi10Mg and Al-Mg-Sc-Zr alloy powders exhibit several reflections typical of the face-centered cubic aluminum phase (Fig. 7). In the case of AlSi10Mg, reflections related to the eutectic Si phase are also visible (Fig. 7a). Interestingly, the AlSi10Mg specimens show a higher relative intensity of the Al (200) Bragg peak compared to the raw powder. This suggests a texture with {200} planes parallel to the sample surface, potentially indicating preferential solidification in the ⟨100⟩ direction perpendicular to the sample surface. This texturing phenomenon in laser melted grains is attributed to the thermal dissipation gradient and has been reported in various studies on AlSi10Mg [34–36].

In contrast, there were no significant differences in the phases and texture of the Al-Mg-Sc-Zr samples, including raw powder and samples from horizontal and vertical building directions (Fig. 7b). The detected diffraction peaks indicate a higher intensity of the {111} peaks compared to the {200} peaks, unlike AlSi10Mg, although both alloys primarily consist of aluminum. The diffractogram resembles that of an isotropic material, comparable to standard aluminum alloys. Similar results were reported by Li et al. [37] and Martucci et al. [38], where PBF-LB samples also exhibited a (111) orientation after processing. This comparison of the ratios of the intensity of the strongest peaks, {111}/{200}, in the powder versus the PBF-LB builds suggests that texture development in the case of Al-Mg-Sc-Zr is relatively weak.

3.2. Mechanical properties

The use of miniaturized AM tensile specimens has been instrumental in conducting a series of tensile tests to determine the mechanical properties of both alloys. While these miniaturized specimens facilitate comparisons between different alloys within the same study and enable in-situ response studies, it's important to note that the results obtained may not be directly comparable to literature results obtained with standard macro specimens.

The tensile tests conducted demonstrate exceptional mechanical properties for Al-Mg-Sc-Zr, particularly in the horizontal building direction, where it outperforms AlSi10Mg by doubling the UTS values. Fig. 8a illustrates one engineering stress-strain curve for each material direction. As evidenced in previous sections, Al-Mg-Sc-Zr exhibits a finer microstructure, a higher number of precipitates, and smaller pores compared to AlSi10Mg. While the building direction does not appear to have a significant impact on the UTS results, as also observed by Kempen et al. [4], deformation to failure appears to be higher for the horizontal building direction (Fig. 10b) in both materials, albeit with a large variation that prevents a definitive conclusion regarding significant differences.

Furthermore, in this study, Al-Mg-Sc-Zr also demonstrates a near-isotropic mechanical behavior during static loading (Fig. 8b), consistent with previous reports by Best et al. [39]. Despite some scatter due to high porosity, the materials exhibit overlap in the values of the vertical and horizontal directions. However, differences in elongation appear to

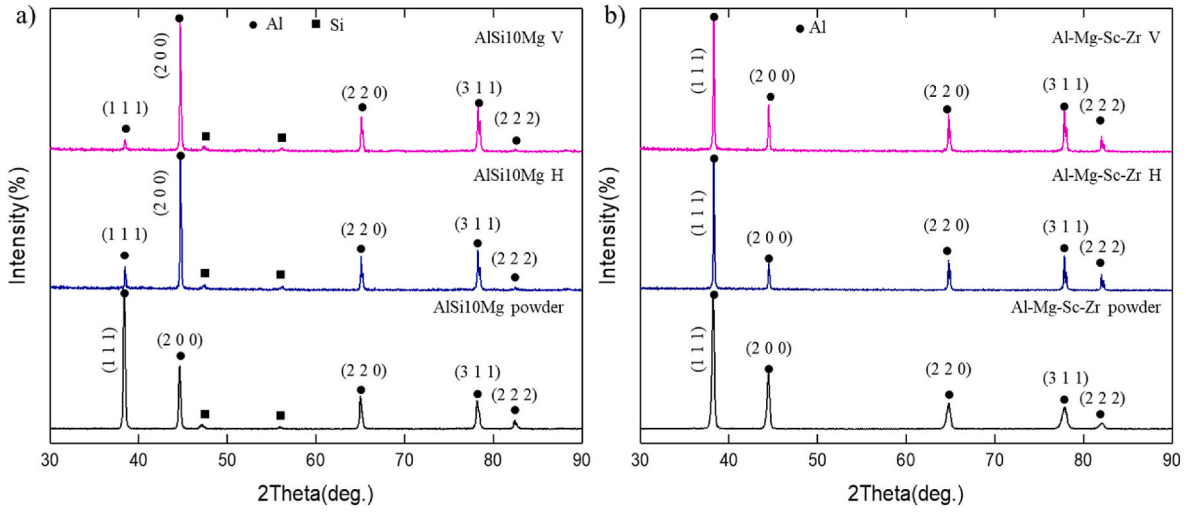

Fig. 7. Phase identification by X-ray diffraction (XRD) of the metal powders, specimens built in horizontal (H) direction and specimens built in vertical (V) direction for both a) AlSi10Mg and b) Al-Mg-Sc-Zr materials.

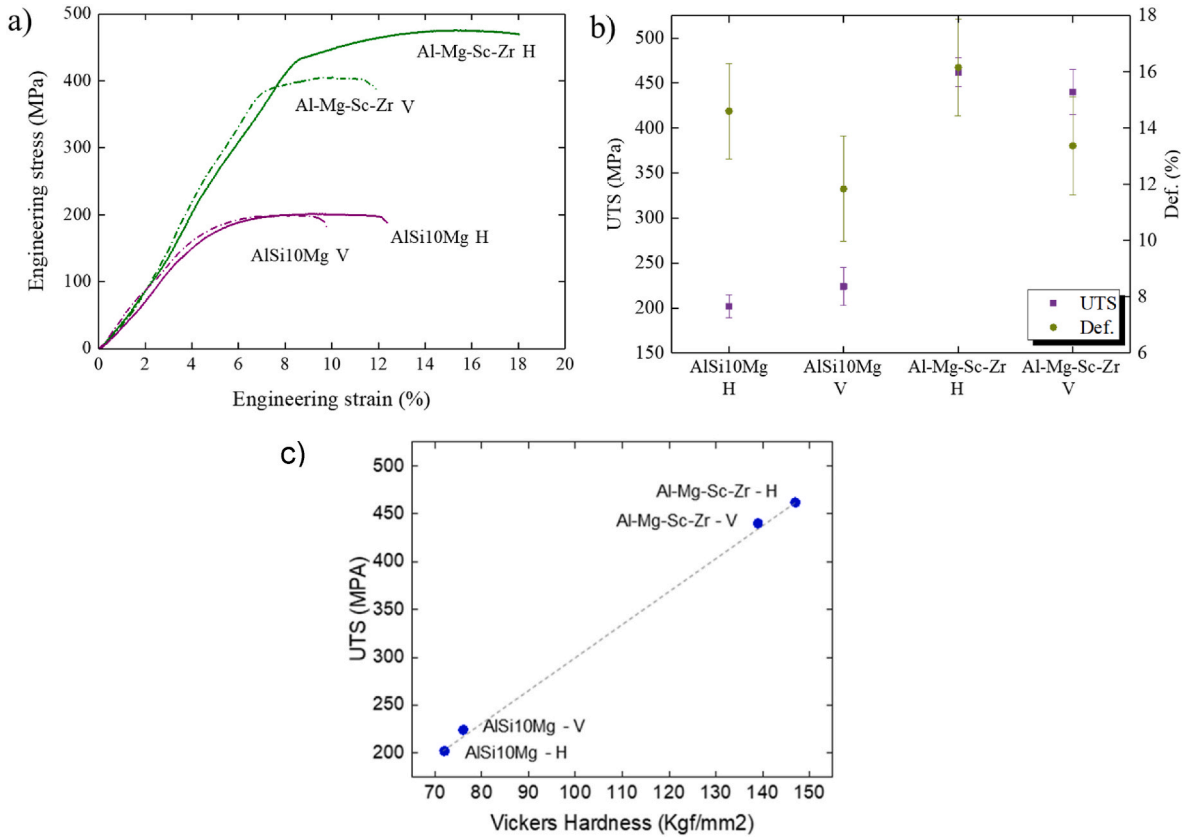

Fig. 8. (a) Stress-strain engineering curves for one specimen of each type: AlSi10Mg and Al-Mg-Sc-Zr in horizontal (H) and vertical (V) building directions. (b) UTS and elongation at break values, including the standard deviation of each datapoint. (c) Vickers hardness to ultimate tensile strength (UTS) correlation.

be more pronounced than differences in UTS, confirming previous observations by Tang and Pistorius [40], who noted differences between the two orientations regarding initial plastic flow and final elongation to failure.

Additionally, the correlation between Vickers hardness and UTS values is depicted in Fig. 8c. As noted by Shakil et al. [17], the strain hardening effect was not accounted for in the hardness-strength correlation factor $C_1 = \frac{\sigma}{HV}$, assuming the material is fully in the plastic domain. Consistent with the tensile test results, the Vickers hardness values for Al-Mg-Sc-Zr are almost twice those for AlSi10Mg, with average values of 142 and 75 HV30, respectively. Thus, based on both literature and experimental evidence, it is shown that the layering process of the PBF-LB is not expected to contribute significantly to differences in yield strength, tensile strength, and elastic modulus.

Previously reported UTS values for AlSi10Mg specimens are 289 MPa and 358 MPa for the vertical and horizontal directions, respectively, with an associated elongation to failure of less than 3.9% [41] In contrast, the UTS values found in this study (Fig. 8) are significantly lower, although the elongation to failure is much higher. The static properties reported for Al-Mg-Sc-Zr in the literature are similar to the values obtained in this study, although the UTS after heat treatment reported in Ref. [42] is slightly higher. It appears that the elastic to plastic transition is better defined (i.e., more localized) in Al-Mg-Sc-Zr than in AlSi10Mg, as observed in Fig. 8a.

The comparison of the miniaturized tensile specimens results with values from macro tests found in the literature indeed showed some differences. However, these differences may well be attributed to variations in heat treatment, porosity level, or grain size instead of specimen geometry. In this study, the AlSi10Mg specimens were subjected to stress relief, and the Al-Mg-Sc-Zr specimens to stress relief and precipitation hardening treatment. In fact, AlSi10Mg specimens heat treated for 2 h at 450 °C are reported to have UTS values below 300 MPa and high

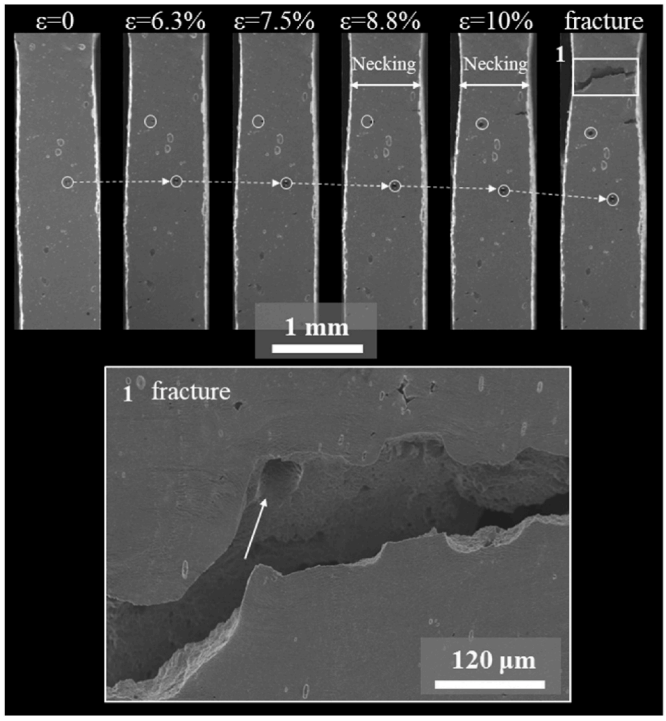

Fig. 9. In-situ test of AlSi10Mg in horizontal building direction (top). The necking formed (at elongation of 8.8 and 10%) before fracture is indicated. Dotted arrows show the displacement of a superficial defect during the test. Detail picture of the crack (bottom). The single arrow indicates an internal pore on the fracture surface.

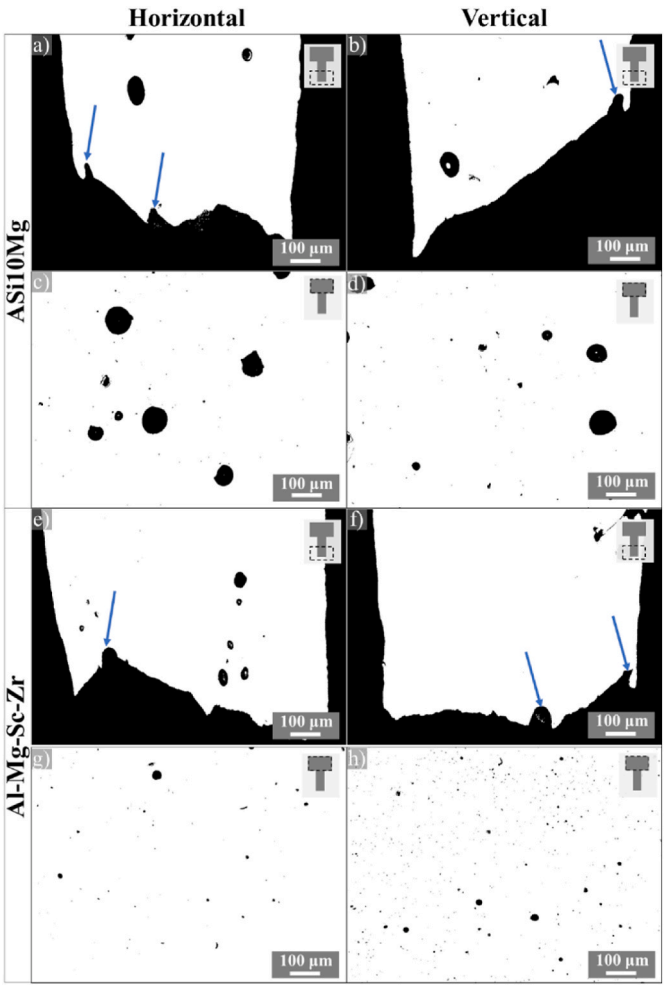

Fig. 10. Porosity in the crack area of AlSi10Mg and AlSi10Mg in the (a,e) horizontal and (b,f) vertical building direction. Porosity in the clamped area in the (c, g) horizontal and (d,h) vertical building direction. The blue arrows indicate voids located at the crack path. (For interpretation of the references to colour in this figure legend, the reader is referred to the Web version of this article.)

elongations to failure (>15%) [16]. Moreover, the as-received values of UTS usually decrease for AlSi10Mg when applying heat treatment, which is attributed to microstructural coarsening [30]. Hardness values found in the literature exhibit higher values than those obtained from the tests, indicating that the studied material also presents a coarser microstructure, fewer precipitates, or higher porosity, leading to worse mechanical properties.

As a result, the deviation in mechanical properties between the AlSi10Mg in this study and the literature may have multiple causes, which does not disqualify the use of miniaturized tensile specimen testing.

One of the main advantages of the tensile tests using miniaturized specimens is the possibility of carrying out in-situ tests to study the role of pores in the fracture behavior. Representative series of images for AlSi10Mg at different amounts of deformation are shown in Fig. 9. The surface porosity, which plays an important role in fracture mechanics, was monitored during the test. Here, the material deforms while cracks initiate and propagate perpendicularly to the building direction, and necking is observed just before fracture. The locations where the largest pores are visible at the surface are not those where fractures occur. It appears that internal pores, which cannot be observed in these SEM images, caused the specimen to fracture at a different location.

Additionally, a small surface crack occurring at $\varepsilon = 8.8$ %, which is

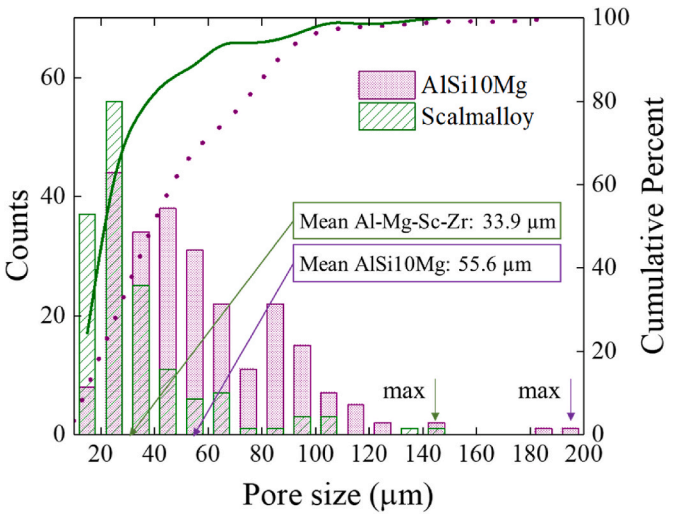

Fig. 11. Porosity distribution measured in specimens of both building directions for AlSi10Mg and Al-Mg-Sc-Zr.

clearly visible at $\varepsilon = 10\%$ and after fracture, is not responsible for the fracture itself, indicating that the toughness of the material is sufficient to withstand a certain degree of porosity. For example, the toughness value (KIC) of PBF-LB processed AlSi10Mg alloy was found to be close to 40 MPa $m^{1/2}$ by Hitzler et al. [43], which clearly suffices. The detailed view of the fracture surface (Fig. 9, bottom) reveals one of the internal pores (indicated by an arrow) that may have caused the initiation of the fracture. The Al-Mg-Sc-Zr specimens exhibit similar behavior to that of the AlSi10Mg shown in Fig. 9.

3.3. Porosity and fractographic analysis

The optical micrographs in Fig. 10 depict the superficial pores on a polished surface, near the crack, and in the clamped areas of both horizontal and vertical building directions. Since the images were captured after the tensile test, the pores close to the crack appear elongated, resulting from the plastic deformation in this zone.

The small spherical pores observed on the specimens can be attributed to overheating and gas entrapped during the melting process. This type of pore is typically referred to as metallurgical or hydrogen pores [10]. The gas entrapped in the pores may originate from the powder bed or from powder reactions. Both alloys contain Mg, which can also be evaporated by the heat applied with the laser source. Therefore, optimization of energy density is necessary to avoid lack of fusion (resulting from too low heat input) and overheating of the molten material (resulting from too high heat input), which can lead to lack-of-fusion pores or metallurgical pores, respectively [44]. Visually, AlSi10Mg specimens exhibit more and larger pores than Al-Mg-Sc-Zr. The crack views (Fig. 10a, b, e, and f) show how the crack changes direction towards the pores, as indicated in the figures by blue arrows.

The mean and maximum pore sizes, as indicated in the histograms of Fig. 11, are derived from the micrographs of the polished clamped areas shown in Fig. 10. Only micrographs of the clamped area are considered for the calculation to prevent the size and shape parameters from being affected by distorted porosity due to the plastic deformation produced in the gauge section of the tensile test.

The pore size distribution plot (Fig. 11) highlights clear differences between the studied materials. AlSi10Mg exhibits a higher mean pore size than Al-Mg-Sc-Zr, with values of 55.6 µm and 33.9 µm, respectively. While this was already observed in the micrographs in Figs. 4, 5 and 10, the cumulative distribution also reveals that the pore size values vary much more in AlSi10Mg than in Al-Mg-Sc-Zr. In the latter, more than 80% of the pores are sized below 40 µm, while in AlSi10Mg, the pore size

Table 3
Morphology f_{shape} index and maximum size of pores measured from the surface of the specimens both in horizontal and vertical building directions. The values and standard deviations are calculated from samples of about 200 pores.

Materials	Build direction	f_{shape} (AR^{-1})	*Max Pore (μm)*
AlSi10Mg	horizontal	0.77 ± 0.16	121.5
	vertical	0.81 ± 0.16	196.5
Al-Mg-Sc-Zr	horizontal	0.83 ± 0.16	145.7
	vertical	0.78 ± 0.16	101.9

is distributed over a much wider range of 20 μm–100 μm.

The larger pores encountered in AlSi10Mg might have a strong influence on the mechanical properties. However, in addition to the pore size, the shape of the pores is also a key parameter to investigate. Irregular pores with sharp ends will be more likely to act as crack initiators than rounded pores. Aboulkhair et al. [45] compared the mechanical properties of as-built, heat-treated PBF-LB AlSi10Mg samples with a die-cast alloy. The UTS decreases from 333 MPa to 292 MPa after the heat treatment while the elongation increases from 1.4% to 3.9% in the heat-treated specimens. These values are comparable to the die-cast material, which exhibits a UTS of 320 MPa and elongation of 3%. It appears that the mechanical properties of the PBF-LB and conventionally manufactured specimens have similar properties, despite the porosity level. In general terms, porosity affects more severely the ductility of the material, its ability to deform, than resistance. From that point of view, if the final shape is reached, (no secondary deformation is required to make the part) it is not critical that it has pores if the strength of the component is reached.

Table 3 shows the values of the f_{shape} index, which is the inverse aspect ratio (AR) value that quantifies the pore shape. A value close to 1 represents a spherical pore. The f_{shape} values for both materials are very similar and between 0.77 and 0.83, implying a high level of sphericity of the pores. Al-Mg-Sc-Zr specimens built in the horizontal direction exhibit a relatively high value, which in combination with the low pore size of this material will be favorable for the mechanical properties. The maximum pore size, which is shown in the final column of Table 3, might influence the mechanical properties. In this case, these large pores are caused by overheating, as can be concluded from the spherical shape of the pores. It is expected that a lower energy density would reduce this number considerably.

Fracture mechanics and crack propagation are strongly dependent on the size, shape, and distribution of pores, which can accelerate crack initiation and propagation. Fractography of broken samples shows the presence of surface and/or sub-surface pores that likely contributed to the failure. In Fig. 12, the internal large and spherical pores that were present on the crack propagation path and fracture surface are shown. As was also observed in Fig. 10, AlSi10Mg again shows the largest pores and the largest number of pores.

When loading the specimens built in horizontal and vertical directions, the static force is applied parallel and perpendicular to the building direction, and therefore to the direction of growth, as shown in Fig. 13a and b, respectively. Although anisotropy was not found in the studied literature on these materials, the results of the present work suggest a tendency toward longer elongation of specimens built in the horizontal direction (Fig. 8b). For the horizontal building direction, Fig. 13b, the force is applied perpendicularly to the building direction. In that case, it is more difficult for the crack to propagate along the melt

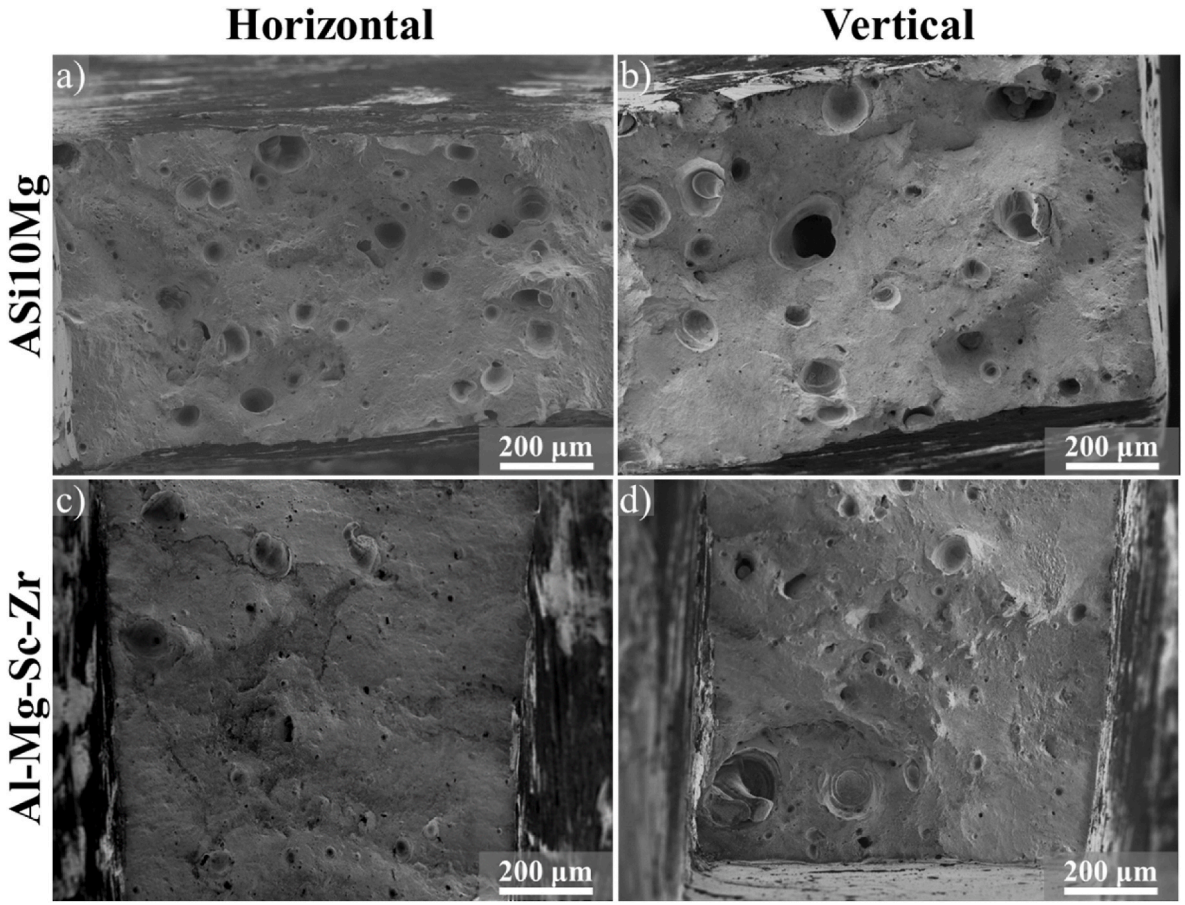

Fig. 12. Internal porosity on the fracture surfaces of the tensile specimens: (a) AlSi10Mg in H building direction, (b) AlSi10Mg in V building direction, (c) Al-Mg-Sc-Zr in H building direction and (d) Al-Mg-Sc-Zr in V building direction. Note that the pore shape might be distorted towards an ellipsoid shape by the plasticity of the tensile test.

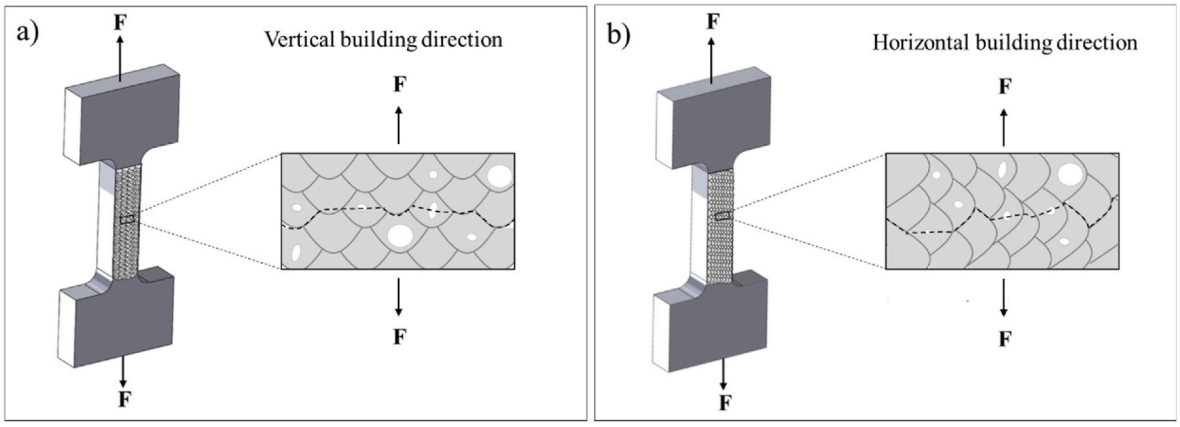

Fig. 13. Crack propagating through the melt pool boundaries when applying a tensile load (F): (a) Vertical building direction and parallel to the applied load (F). (b) Horizontal building direction and perpendicular to the applied load (F).

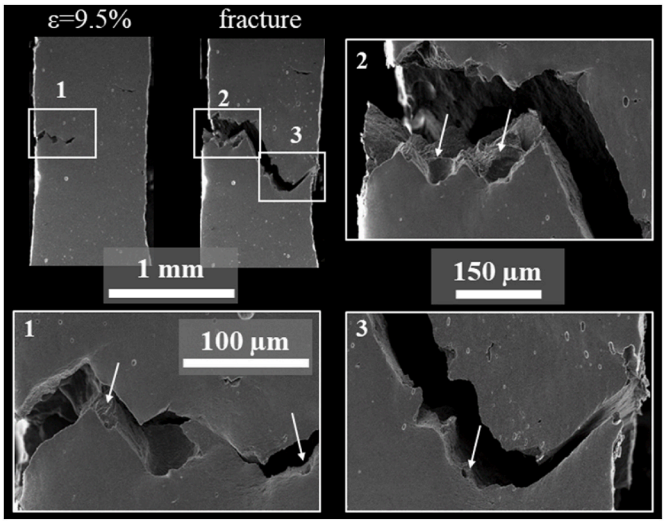

Fig. 14. In-situ test of AlSi10Mg in vertical building direction. The crack is observed at an elongation value of 9.5% and fracture. The arrow indicates internal pores on the fracture surface.

pool boundaries than for the vertical building direction as indicated by the dotted line.

Nonetheless, from the analysis of the fracture surfaces, it was found that the crack can also propagate both along differently sized grains (Fig. 12), leaving dimples of various sizes, and can also propagate along large pores (Fig. 11), which deform to an ellipsoid shape due to plastic deformation. The tensile test curves show a considerable amount of plastic deformation. This suggests that the material is capable of plastic deformation despite the presence of the pores. Apparently, the pores do not cause a crack to grow, even though the stress is at the level of the yield point. Due to the size of the tensile specimens, only a few melt pools are supporting the load (circa ten melt pools in a width of 1 mm), and any large pore can be decisive to provoke failure.

Fig. 14 shows the crack opening in a direction perpendicular to the melt pool growing direction. The crack growth path appears to change drastically, leaving sharp surfaces promoted by internal pores and microstructure, as indicated by the arrows. Thus, in metal PBF-LB materials, cracks propagate along the intersections of grains and melt pool boundaries, as well as in the presence of pores, especially the irregularly shaped ones as shown in Fig. 13.

Porosity development during the PBF-LB process is critical for improving mechanical behavior. The type of porosity observed is associated with high energy and gas trapping, thus pore formation is associated with gas solubility and melt pool surface tension. This can be attributed to trapping of argon from the build chamber due to the active flow of molten metal or to dissolved hydrogen degassed from the powders at the time of melting. In this case, two aluminum alloys processed with optimized process parameters revealed a considerable porosity difference. It seems that porosity is more prone to form in AlSi10Mg than in Al-Mg-Sc-Zr, or at least the energy density must be decreased for the first material, as overheating causes most of the porosity.

After a closer look at the fracture surfaces of the tensile tests, a ductile fracture micro-mechanism is observed (Fig. 15). The fracture surfaces of both materials are covered by dimples, although this is more predominant in AlSi10Mg. This material presents two different sizes of dimples, as indicated by the dashed rectangles, in agreement with the different microstructural zones. Microvoid coalescence (MVC) is the mechanism of ductile transgranular fracture that is observed here. Often, both ductile and brittle fracture occur together on a single fracture surface. In fact, Al-Mg-Sc-Zr exhibits quasi-cleavage areas indicated by dotted arrows. These cleavage facets form steps along the crystallographic planes of the material. They are more common in the vertical building direction, as the melt pools form perpendicular to the applied load, so the crack can also propagate through the melt pool boundaries. As observed, a few micropores are found in the fracture surface, which probably also contributed to the crack propagation.

4. Conclusions

In this work, near net shape miniaturized tensile specimens of AlSi10Mg and Al-Mg-Sc-Zr were produced by PBF-LB to study their processability after a powder drying treatment and to examine their mechanical properties. The conclusions drawn from this study are as follows.

1. **Microstructural Differences:** The addition of scandium in the AM-specific material Al-Mg-Sc-Zr resulted in a strengthened microstructure caused by precipitation hardening, with an average grain size of 2.3 µm. In contrast, the AlSi10Mg alloy exhibited a coarser microstructure with an average grain size of 8.0 µm and longer grains along the melt pools.
2. **Superior Mechanical Properties of Al-Mg-Sc-Zr:** Al-Mg-Sc-Zr showed superior mechanical properties compared to AlSi10Mg, with Ultimate Tensile Strength (UTS) exceeding 450 MPa, whereas AlSi10Mg exhibited UTS values of around 225 MPa. Additionally, Al-Mg-Sc-Zr demonstrated twice the hardness of AlSi10Mg. Although the elongation to failure was similar for both materials, at approximately 12–16%, the printing orientation slightly affected elongation due to the presence of large pores.

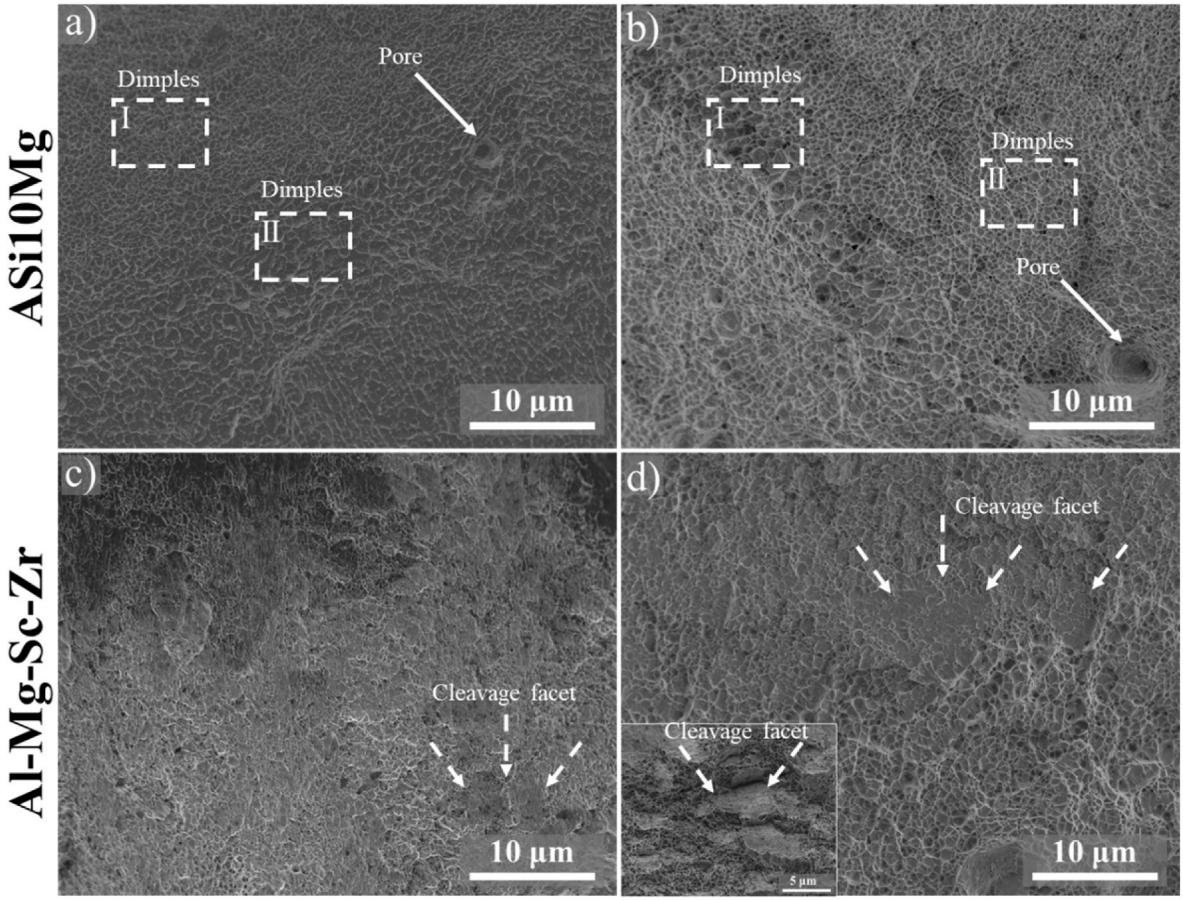

Fig. 15. Fracture surfaces of: (a) AlSi10Mg horizontal, (b) AlSi10Mg vertical, (c) Al-Mg-Sc-Zr horizontal, (d) Al-Mg-Sc-Zr vertical. Dimple zones I and II of various sizes in AlSi10Mg are indicated with dotted rectangles. The continuous arrows indicate the voids, the dotted arrows indicate the cleavage areas observed in Al-Mg-Sc-Zr.

3. **Impact of Porosity:** The level of porosity in AlSi10Mg was not only high but also contained large pores that were detrimental to mechanical properties. This could be attributed to overheating of the molten material during printing, which promotes pore coalescence and growth. The average pore sizes for AlSi10Mg and Al-Mg-Sc-Zr were 55.6 µm and 33.9 µm, respectively.
4. **Fracture Mechanics Analysis:** Both AlSi10Mg and Al-Mg-Sc-Zr exhibited ductile fracture surfaces, although the latter displayed cleavage facets due to high localized strength caused by small grain size. Internal pores were found to play a crucial role in the formation and propagation of cracks.
5. **Suitability of Miniaturized Tensile Specimens:** Miniaturized tensile specimens proved suitable for characterizing AM parts, allowing the mechanical properties of small features in complex parts to be studied. In-situ SEM tensile tests provided insights into fracture behavior. While results from micro specimens may not be directly comparable with macro specimens due to sensitivity to large pores, they still allow for comparison between different alloys within the same study.

Overall, the study highlights the importance of microstructural optimization, porosity control, and fracture mechanics analysis in understanding and improving the mechanical performance of AM materials.

Data availability statement

The raw/processed data required to reproduce these findings cannot be shared at this time as the data also forms part of an ongoing study.

Declaration of competing interest

The authors declare the following financial interests/personal relationships which may be considered as potential competing interests: Prof. Tiedo Tinga reports financial support was provided by Dutch Research Council. If there are other authors, they declare that they have no known competing financial interests or personal relationships that could have appeared to influence the work reported in this paper.

Acknowledgments

This research has been supported by the Dutch Research Council under project number 438-13-207, named “Sustainability Impact of New Technology on After sales Service supply chains (SINTAS)". The authors are grateful to Ralph Haagsma and Marc de Smit from the Netherlands Aerospace Centre (NLR), and Nick Helthuis from the University of Twente for their contribution to this paper.

References

[1] Frazier WE. Metal additive manufacturing: a review. J Mater Eng Perform 2014;23 (6):1917–28. https://doi.org/10.1007/s11665-014-0958-z.
[2] Buchbinder D, Schleifenbaum H, Heidrich S, Meiners W, Bültmann J. High power selective laser melting (HP SLM) of aluminum parts. Phys Procedia 2011;12:271–8. https://doi.org/10.1016/j.phpro.2011.03.035. PART 1.
[3] Thijs L, Kempen K, Kruth JP, Van Humbeeck J. Fine-structured aluminium products with controllable texture by selective laser melting of pre-alloyed AlSi10Mg powder. Acta Mater 2013;61(5):1809–19. https://doi.org/10.1016/j.actamat.2012.11.052.

[4] Kempen K, Thijs L, Van Humbeeck J, Kruth JP. Mechanical properties of AlSi10Mg produced by selective laser melting. Phys Procedia 2012;39:439–46. https://doi.org/10.1016/j.phpro.2012.10.059.

[5] Montero Sistiaga ML, et al. Changing the alloy composition of Al7075 for better processability by selective laser melting. J Mater Process Technol 2016;238:437–45. https://doi.org/10.1016/j.jmatprotec.2016.08.003.

[6] Zhou S, et al. Effect of Sc on microstructure and mechanical properties of as-cast Al-Mg alloys. Mater Des 2016;90:1077–84. https://doi.org/10.1016/j.matdes.2015.10.132.

[7] Bayoumy D, Kan W, Wu X, Zhu Y, Huang A. The latest development of Sc-strengthened aluminum alloys by laser powder bed fusion. J Mater Sci Technol 2023;149:1–17. https://doi.org/10.1016/j.jmst.2022.11.028.

[8] Aboulkhair NT, Maskery I, Tuck C, Ashcroft I, Everitt NM. On the formation of AlSi10Mg single tracks and layers in selective laser melting: microstructure and nano-mechanical properties. J Mater Process Technol 2016;230:88–98. https://doi.org/10.1016/j.jmatprotec.2015.11.016.

[9] Cordova L, Campos M, Tinga T. Assessment of moisture content and its influence on laser beam melting feedstock. Milan: EURO PM2017 - Congress & Exhibition; 2017.

[10] Aboulkhair NT, Everitt NM, Ashcroft I, Tuck C. Reducing porosity in AlSi10Mg parts processed by selective laser melting. Addit Manuf 2014;1:77–86. https://doi.org/10.1016/j.addma.2014.08.001.

[11] Galy C, Le Guen E, Lacoste E, Arvieu C. Main defects observed in aluminum alloy parts produced by SLM: from causes to consequences. Addit Manuf 2018;22:165–75. https://doi.org/10.1016/j.addma.2018.05.005.

[12] Khorasani AM, Gibson I, Ghaderi A, Mohammed MI. Investigation on the effect of heat treatment and process parameters on the tensile behaviour of SLM Ti-6Al-4V parts. Int J Adv Manuf Technol 2019;101(9–12):3183–97. https://doi.org/10.1007/s00170-018-3162-8.

[13] Olakanmi EO. Selective laser sintering/melting (SLS/SLM) of pure Al, Al-Mg, and Al-Si powders: effect of processing conditions and powder properties. J Mater Process Technol 2013;213(8):1387–405. https://doi.org/10.1016/j.jmatprotec.2013.03.009.

[14] Hojjatzadeh SMH, et al. Pore elimination mechanisms during 3D printing of metals. Nat Commun 2019;10(1):1–8. https://doi.org/10.1038/s41467-019-10973-9.

[15] Weingarten C, Buchbinder D, Pirch N, Meiners W, Wissenbach K, Poprawe R. Formation and reduction of hydrogen porosity during selective laser melting of AlSi10Mg. J Mater Process Technol 2015;221:112–20. https://doi.org/10.1016/j.jmatprotec.2015.02.013.

[16] Li XP, O'Donnell KM, Sercombe TB. Selective laser melting of Al-12Si alloy: enhanced densification via powder drying. Addit Manuf 2016;10:10–4. https://doi.org/10.1016/j.addma.2016.01.003.

[17] Shakil SI, et al. Insights into laser powder bed fused Scalmalloy®: investigating the correlation between micromechanical and macroscale properties. J Mater Res Technol 2023;25:4409–24. https://doi.org/10.1016/j.jmrt.2023.06.228.

[18] Zheng P, et al. On the standards and practices for miniaturized tensile test – a review. Fusion Eng Des 2020;161(September):112006. https://doi.org/10.1016/j.fusengdes.2020.112006.

[19] Torralba JM, Esteban L, Bernardo E, Campos M. Understanding contribution of microstructure to fracture behaviour of sintered steels. Powder Metall 2014;57(5):357–64. https://doi.org/10.1179/1743290114Y.0000000119.

[20] Strondl A, Lyckfeldt O, Brodin H, Ackelid U. Characterization and control of powder properties for additive manufacturing. JOM 2015;67(3):549–54. https://doi.org/10.1007/s11837-015-1304-0.

[21] Cordova L, Campos M, Tinga T. Revealing the effects of powder reuse for selective laser melting by powder characterization. JOM 2019;71(3):1062–72. https://doi.org/10.1007/s11837-018-3305-2.

[22] Read N, Wang W, Essa K, Attallah MM. Selective laser melting of AlSi10Mg alloy: process optimisation and mechanical properties development. Mater Des 2015;65:417–24. https://doi.org/10.1016/j.matdes.2014.09.044.

[23] Maamoun AH, Elbestawi M, Dosbaeva GK, Veldhuis SC. Thermal post-processing of AlSi10Mg parts produced by Selective Laser Melting using recycled powder. Addit Manuf 2018;21:234–47. https://doi.org/10.1016/j.addma.2018.03.014.

[24] Spierings AB, Dawson K, Voegtlin M, Palm F, Uggowitzer PJ. Microstructure and mechanical properties of as-processed scandium-modified aluminium using selective laser melting. CIRP Ann - Manuf Technol 2016;65(1):213–6. https://doi.org/10.1016/j.cirp.2016.04.057.

[25] Li W, et al. Effect of heat treatment on AlSi10Mg alloy fabricated by selective laser melting: microstructure evolution, mechanical properties and fracture mechanism. Mater Sci Eng, A 2016;663:116–25. https://doi.org/10.1016/j.msea.2016.03.088.

[26] Spierings AB, et al. Microstructural features of Sc- and Zr-modified Al-Mg alloys processed by selective laser melting. Mater Des 2017;115:52–63. https://doi.org/10.1016/j.matdes.2016.11.040.

[27] Schmidtke K, Palm F, Hawkins A, Emmelmann C. Process and mechanical properties: applicability of a scandium modified Al-alloy for laser additive manufacturing. Phys Procedia 2011;12(1):369–74. https://doi.org/10.1016/j.phpro.2011.03.047. PART.

[28] Bayat M, et al. Keyhole-induced porosities in laser-based powder bed fusion (L-PBF) of Ti6Al4V: high-fidelity modelling and experimental validation. Addit Manuf 2019;30:100835. https://doi.org/10.1016/j.addma.2019.100835.

[29] Kan WH, Nadot Y, Foley M, Ridosz L, Proust G, Cairney JM. Factors that affect the properties of additively-manufactured AlSi10Mg: porosity versus microstructure. Addit Manuf 2019;29:100805. https://doi.org/10.1016/j.addma.2019.100805.

[30] Liu X, Zhao C, Zhou X, Shen Z, Liu W. Microstructure of selective laser melted AlSi10Mg alloy. Mater Des 2019;168:107677. https://doi.org/10.1016/j.matdes.2019.107677.

[31] Spierings AB, Dawson K, Uggowitzer PJ, Wegener K. Influence of SLM scan-speed on microstructure, precipitation of Al3Sc particles and mechanical properties in Sc- and Zr-modified Al-Mg alloys. Mater Des Feb. 2018;140:134–43. https://doi.org/10.1016/J.MATDES.2017.11.053.

[32] Turani M, Jannic W, Esteves PDB, Tosoratti E, Spierings A, Bambach M. Investigating the influence of iron content on the microstructure and mechanical properties of a high strength Al-alloy for additive manufacturing. In: Wagstaff S, editor. Light metals 2024. Cham: Springer Nature Switzerland; 2024. p. 1141–7.

[33] Dorin T, Ramajayam M, Vahid A, Langan T. "Aluminium scandium alloys," fundamentals of aluminium metallurgy: recent advances. Jan. 2018. p. 439–94. https://doi.org/10.1016/B978-0-08-102063-0.00012-6.

[34] Lam LP, Zhang DQ, Liu ZH, Chua CK. Phase analysis and microstructure characterisation of AlSi10Mg parts produced by Selective Laser Melting. Virtual Phys Prototyp 2015;10(4):207–15. https://doi.org/10.1080/17452759.2015.1110868.

[35] Zhang C, Zhu H, Qi Y, Zeng X. The effect of annealing on microstructure and mechanical properties of selective laser melting AlSi10Mg. IOP Conf Ser Mater Sci Eng 2019;538(1). https://doi.org/10.1088/1757-899X/538/1/012023.

[36] Liu YJ, Liu Z, Jiang Y, Wang GW, Yang Y, Zhang LC. Gradient in microstructure and mechanical property of selective laser melted AlSi10Mg. J Alloys Compd 2018;735:1414–21. https://doi.org/10.1016/j.jallcom.2017.11.020.

[37] Li R, Chen H, Zhu H, Wang M, Chen C, Yuan T. Effect of aging treatment on the microstructure and mechanical properties of Al-3.02Mg-0.2Sc-0.1Zr alloy printed by selective laser melting. Mater Des 2019;168:107668. https://doi.org/10.1016/j.matdes.2019.107668.

[38] Martucci A, et al. Low-power laser powder bed fusion processing of Scalmalloy. Materials 2022;15(9). https://doi.org/10.3390/ma15093123.

[39] Best JP, Maeder X, Michler J, Spierings AB. Mechanical anisotropy investigated in the complex SLM-processed Sc- and Zr-modified Al–Mg alloy microstructure. Adv Eng Mater 2019;21(3):1–6. https://doi.org/10.1002/adem.201801113.

[40] Tang M, Pistorius PC. Anisotropic mechanical behavior of AlSi10Mg parts produced by selective laser melting. JOM 2017;69(3):516–22. https://doi.org/10.1007/s11837-016-2230-5.

[41] Mower TM, Long MJ. Mechanical behavior of additive manufactured, powder-bed laser-fused materials. Mater Sci Eng, A 2016;651:198–213. https://doi.org/10.1016/j.msea.2015.10.068.

[42] Spierings AB, Dawson K, Kern K, Palm F, Wegener K. SLM-processed Sc- and Zr-modified Al-Mg alloy: mechanical properties and microstructural effects of heat treatment. Mater Sci Eng, A 2017;701:264–73. https://doi.org/10.1016/j.msea.2017.06.089.

[43] Hitzler L, et al. Fracture toughness of L-PBF fabricated aluminium–silicon: a quantitative study on the role of crack growth direction with respect to layering. Progress in Additive Manufacturing 2020;5(3):259–66. https://doi.org/10.1007/s40964-020-00113-x.

[44] Kempen K, Thijs L, Van Humbeeck J, Kruth JP. Processing AlSi10Mg by selective laser melting: parameter optimisation and material characterisation. Mater Sci Technol 2015;31(8):917–23. https://doi.org/10.1179/1743284714Y.0000000702.

[45] Aboulkhair NT, Maskery I, Tuck C, Ashcroft I, Everitt NM. The microstructure and mechanical properties of selectively laser melted AlSi10Mg: the effect of a conventional T6-like heat treatment. Mater Sci Eng, A 2016;667:139–46. https://doi.org/10.1016/j.msea.2016.04.092.